

Exfoliation of layered Na-ion anode material $\text{Na}_2\text{Ti}_3\text{O}_7$ for enhanced capacity and cyclability

Maria A. Tsiamtsouri ^{ab}, Phoebe K. Allan ^{acd}, Andrew J. Pell ^{a†}, Joshua M. Stratford ^a, Gunwoo Kim ^{ab}, Rachel N. Kerber ^a, Pieter M. Magusin ^a, David A. Jefferson ^a, Clare P. Grey ^{ab*}

a Chemistry Department, University of Cambridge, Lensfield Road, Cambridge, CB2 1EW, UK

b Cambridge Graphene Centre, University of Cambridge, Cambridge, CB3 0FA, UK

c Gonville and Caius College, Trinity Street, Cambridge, CB2 1TA, UK

d Diamond Light Source Ltd., Harwell Science and Innovation Campus, Didcot, OX11 0DE, UK

† Current address: Department of Material and Environmental Chemistry, Stockholm University, Svante Arrhenius Väg 16 C, Stockholm, 106 91, Sweden

*E-mail: cpg27@cam.ac.uk

ABSTRACT: We report the exfoliation of layered $\text{Na}_2\text{Ti}_3\text{O}_7$, a promising anode material for Na-ion batteries, and restacking using HNO_3 and NaOH to form $\text{H}[\text{Ti}_3\text{O}_7]$ and $\text{Na}(x)[\text{Ti}_3\text{O}_7]$ compositions, respectively. The materials were characterised by a range of techniques (SEM, TEM, solid-state NMR, XRD, PDF). Although the formation of aggregated nanoparticles is favoured under acidic restacking conditions, the use of basic conditions can lead to control over the adherence between the exfoliated layers. Pair distribution function (PDF) analysis confirms that the local TiO_6 connectivity of the pristine material is maintained. The lowest sodium-containing $\text{Na}(1)[\text{Ti}_3\text{O}_7]$ phase, which is the stable product upon Na^+ leaching after consecutive washing steps, displays the best performance among the compositions studied, affording a stable reversible capacity of about 200 mAh.g^{-1} for 20 cycles at a $C/20$ rate. Washing removes the excess of ‘free/reactive’ Na^+ , which otherwise forms inactive Na_2CO_3 in the insufficiently-washed compositions.

Introduction

The discovery of atomically-thick graphene has recently aroused great interest in the properties and phenomena exhibited by two-dimensional (2D) materials, which in general can be considered as the exfoliation products of layered structures to form either single or few layers. The exfoliation of layered structures to individual or few nanosheets can be advantageous for applications requiring high surface activity, such as catalysis, electrochemistry and photoelectrochemistry.^[1, 2]

In the extended family of layered inorganic structures, including metal oxides, metal chalcogenides (for example, reduced TiS_2 , MoS_2 and WS_2), LiCoO_2 and others,^[1, 2] interlayer counterions are often required to preserve/maintain the electroneutrality. This is advantageous for ion-exchange properties, but makes their exfoliation to generate individual layers more challenging than for graphite^[1, 3, 4], because of the strong Coulombic forces that hold them together.^[1]

In general, Na-ion batteries are considered as a lower-cost alternative to their Li-ion counterparts, which operate in a similar manner. This is in part due to the high natural abundance of sodium, along with the option to use aluminum current collectors on the anode side, instead of the more expensive copper used for Li-ion batteries. One of the key challenges for implementation of the Na-ion technology is related to discovering new anode materials since graphite, the anode of choice for Li-ion batteries, does not show electrochemical activity in Na-ion batteries.^[5, 6] Hard (non-graphiteable) carbon can however reversibly intercalate Na^+ ions via a combined mechanism of Na^+ insertion between the nearly parallel layers and into nanopores but much of this storage takes place close to the sodium-plating voltage, raising potential safety concerns.^[7, 8] Other potential anode materials are also being explored,^[9, 10] among them, a variety of titanium-based structures, but these show low specific capacity in part due to the limited Na storage sites within the host structures.^[9-11] Titanium-based structures are often preferred for various anode applications due to their lack of toxicity and relatively low cost compared to other transition metals, such as cobalt or manganese, and the redox activity of titanium being in the appropriate voltage window.^[12]

Layered $\text{Na}_2\text{Ti}_3\text{O}_7$ is a well-known potential anode material for Na-ion batteries demonstrating good electrochemical

properties at a low intercalation potential of around 0.3 V vs. Na^+/Na .^[13, 14] It is built up of corrugated $(\text{Ti}_3\text{O}_7)^{2-}$ layers (formed by series of corner-sharing tri-octahedral ribbons) and Na^+ ions sitting in the interlayer space. The low intercalation potential of $\text{Na}_2\text{Ti}_3\text{O}_7$ is advantageous when coupled with a high-voltage cathode in a full cell to achieve a higher energy density. For example, $\text{Na}_2\text{Ti}_3\text{O}_7$ nanotubes have recently been tested as anode materials in full-cell batteries using the high-voltage cathode material VOPO_4 ($V = 3.75$ V vs. Na^+/Na), demonstrating promising electrochemical performance.^[15] It is generally believed that reduction of $\text{Na}_2\text{Ti}_3\text{O}_7$ occurs *via* the reversible intercalation of two additional Na^+ ions in the structure, forming $\text{Na}_4\text{Ti}_3\text{O}_7$,^[14] with $2/3$ of the Ti(IV) ions being reduced to Ti(III).^[13] Several studies have attempted to enhance the electrochemical capacity of this material by generating sodium vacancies within the crystal structure^[16] and by fabrication of carefully controlled nanostructures. Recent advances in the field showing promising performance include bottom-up (BU) techniques for growing $\text{Na}_2\text{Ti}_3\text{O}_7$ based structures, such as growth of nanotube arrays^[17], formation of a 3D spider-web architecture assembled by nanotubes^[18], and growth on carbon-coated hollow spheres^[19]. Promising results have also been reported when techniques favouring reduced particle size are used; these include crystalline rods prepared by microemulsion^[20] and microspherical particles prepared by spray-drying^[21]. Limited reports exist for preparing $\text{Na}_2\text{Ti}_3\text{O}_7$ via top-down (TD) facile techniques. It has been recently reported that exfoliation of bulk $\text{Na}_2\text{Ti}_3\text{O}_7$ can be achieved by ion exchange using alkyl ammonium ions. With some Na^+ ions remaining from the parent material, alongside propylamine ions added during the exfoliation process, a mixture of nanosheets and nanoplatelets was formed. This process led to an improvement in the charge storage kinetics and cyclability compared to the bulk material.^[22]

In this study, we sought to entirely exfoliate $\text{Na}_2\text{Ti}_3\text{O}_7$ into nanosheets by complete removal of Na, along with the alkyl ammonium ions used during the process, followed by re-insertion of Na ions to restack the layers in a more disordered fashion. This was envisioned to create additional sites for Na^+ ion insertion, allowing for complete reduction of Ti^{4+} to Ti^{3+} , thus increasing the capacity.^[1-2] In addition, surface effects, as a result from exfoliation to thinner nanosheets,

may favour further enhancement of the electrochemical performance in terms of the rate performance. We explored the effect of the exfoliation/restacking conditions on the structural chemistry, morphology and electrochemical properties of the phases obtained.

Experimental

Synthesis: The pristine layered $\text{Na}_2\text{Ti}_3\text{O}_7$ materials were made by solid-state synthesis, according to previous reports.^[23] Stoichiometric amounts of Na_2CO_3 (Alfa Aesar, anhydrous, 99.5% purity) and TiO_2 (anatase, Sigma Aldrich, 99.8% purity) were ball-milled in isopropanol using a high-energy mill, and after evaporation of the solvent the mixture was sintered at 800 °C for 20 h in air, followed by grinding and a second sintering step under the same conditions. The same synthesis protocol was followed for the $\text{Na}_2\text{Ti}_6\text{O}_{13}$ and Na_2TiO_3 model compounds.

The protonated $\text{H}_2\text{Ti}_3\text{O}_7$ form was made by ion-exchange of pristine $\text{Na}_2\text{Ti}_3\text{O}_7$ via a solvothermal reaction in HNO_3 (aq) in an autoclave at 60 °C for 12 h. The material was isolated by filtration (Durapore PVDF membrane, pore size 0.22 μm , diam. 47 mm), washed with copious deionized (DI) water until neutral pH was achieved, and dried in an oven at 60 °C. The proton analogue $\text{H}_2\text{Ti}_3\text{O}_7$, was then gradually swollen by ion exchange in two steps of increasing size alkyl ammonium ions in aqueous solutions of amines (MA: methylamine and PA: propylamine). Each reaction was performed solvothermally at 120 °C for 48 h in an autoclave, with the concentrations used as reported previously.^[23] The resulting colloidal suspensions were centrifuged at 6000 rpm for 5 min and the precipitates were washed and centrifuged for a further three times, until neutral pH. The MA- Ti_3O_7 and PA- Ti_3O_7 samples were then dried in an oven at 60 °C prior to further characterisation. The final titanate product of amine swelling (PA- Ti_3O_7) was then dispersed in water (0.1 g in 50 ml H_2O), followed by sonication in order to exfoliate to titanate layers/nanosheets. The non-exfoliated material was collected as the precipitate of centrifugation at 6000 rpm for 5 min. The supernatant suspension, containing the dispersed exfoliated nanosheets, was then restacked by mixing with HNO_3 or NaOH aqueous solutions, in 1:1 ratio by volume. After being left overnight to settle, the precipitates were easily separated by centrifugation (3000 rpm, for 3 min). In the

case of restacking by NaOH , the washing procedure of the precipitate was carefully controlled, resulting in different amounts of inserted Na in the exfoliated/restacked samples. All the samples were dried, initially in air at 60 °C and finally at 100 °C in a vacuum oven.

Powder X-ray Diffraction (PXRD) measurements were performed in a reflection mode (Panalytical Empyrean diffractometer, with $\text{Cu K}\alpha$ radiation ($\lambda=1.5406 \text{ \AA}$)).

Transmission electron microscopy (TEM) images were recorded at magnification between 40,000X and 800,000X in a JEOL JEM-3011 electron microscope operated at 300 kV, with objective lens characteristics $C_s = 0.6 \text{ mm}$ and $C_c = 1.2 \text{ mm}$. With a LaB_6 emitter these produced an interpretable resolution limit of 0.17 nm and an absolute information limit of 0.14 nm. Scanning electron microscopic (SEM) images were recorded with a Hitachi S-5500 in lens field emission electron microscope.

Pair Distribution Function (PDF) analysis: Data of the samples, packed into kapton capillaries, were collected at the I15 beamline at Diamond Light Source, Didcot, UK. An X-ray beam of energy of 76 keV ($\lambda = 0.1631 \text{ \AA}$) was used in conjunction with an amorphous silicon area detector (Perkin-Elmer). The sample geometry and the sample-to-detector distance were determined using a CeO_2 standard. The data were converted to intensity vs Q using the Data Analysis Workbench (DAWN).^[24] Standard corrections (background subtraction, Compton scattering, detector effects) were applied, and the data were Fourier transformed to obtain $G(r)$ using the software PDFGetX2 using a Q_{max} of 24 \AA^{-1} .^[25] Refinements against known TiO_2 phases were performed in PDFGui.^[26] Refinements against single-layer models were performed in the Diffpy-CMI complex modeling framework.^[27] The starting model was simulated from supercells of the $\text{Na}_2\text{Ti}_3\text{O}_7$ structure, where all atoms except for a single-layer in the middle of the unit cell were removed. The structure function was simulated from the Debye scattering equation^[28] which was then Fourier transformed over a range of 1–24 \AA^{-1} . The model was refined using a least-squares approach; unit cell parameters, a , b , c and β , an isotropic thermal parameter, U_{iso} , for each atomic species and a scale factor were allowed to refine.

Solid-state NMR: All solid-state ^1H and ^{23}Na NMR spectra were acquired on a 16.4 T

Bruker Avance III spectrometer using a 1.3 mm HX probe head. A rotor-synchronized Hahn-echo (for ^1H) and a single-pulse sequence (for ^{23}Na) were used to acquire magic-angle spinning (MAS) spectra with spinning frequencies of 55-60 kHz, recycle delays of 5 and 5-40 s (for ^1H and ^{23}Na , respectively), and radiofrequency (rf) field strengths of 125 and 140 kHz, respectively. ^1H and ^{23}Na shifts were externally referenced to solid adamantane at 1.87 ppm and solid NaCl at 7.21 ppm, respectively. Simulations of ^{23}Na MAS powder spectra were performed with SIMPSON.^[29]

First-principles calculations: DFT computations were performed using CASTEP with on-the-fly generated pseudopotentials.^[30-32] For the electron-electron exchange and correlation interactions, the functional of Perdew, Burke and Ernzerhof (PBE)^[33-36] was employed. Non-spin-polarized calculations were performed for the geometry optimization of the $\text{Na}_2\text{Ti}_3\text{O}_7$ system. The k-points mesh used was $3\times 3\times 3$ with cutoff energy of 700 eV.

Compositional analysis: For C/H/N analysis, an Exeter analytical CE440 analyser was used. Typically, 1-2 mgs of sample were combusted at 950 °C in oxygen. For the ICP analysis, a Thermo scientific iCAP 7400 OES

instrument was used. Samples were digested at 80 °C for four hours in 2 ml aqua regia. They were then made up to 50 ml using Millipore 18 M water. The ICP was calibrated using 10 ppm and 1 ppm standard samples.

Electrochemical testing was carried out in CR2032 coin cells vs. sodium metal, in a galvanostatic mode. The electrolyte used 1M NaPF_6 in propylene carbonate (PC, >99% Aldrich) and glass fibre (Whatman GF B 55) was used as a separator. The working electrode was prepared by mixing 70% active materials, with 30% carbon Super C-65 (Timcal) and 10% binder (PVdF-HPF copolymer) in NMP in a mortar and pestle. The mixed slurries were casted on copper foil using the doctor blade technique. A cell containing only carbon was also prepared for comparison reasons in a similar way, but the electrode slurry consisted of 70% carbon Super C-65 (Timcal) and 30% binder to ensure adequate adhesion to the copper foil and between particles. The laminates were vacuum dried at 100 °C for 12 h prior to punching and pressing the electrodes, followed by further drying at 100 °C under vacuum for 12 h. The cells were assembled in a glovebox under argon atmosphere ($\text{O}_2 < 0.1$ ppm and $\text{H}_2\text{O} < 0.1$ ppm). The typical electrode loading was 20-25 mg.

Results and Discussion

Pristine $\text{Na}_2\text{Ti}_3\text{O}_7$ was made by solid-state synthesis, as reported previously^[13], and was characterized by PXRD (SI, Figure S1 and Table S1, also included in *Figure 1B* in red) and ^{23}Na NMR (SI, Figure S2 and Table S2, spectrum also shown in *Figure 3C*). SEM shows that the pristine material comprises well-shaped nanorods of approximately 2.5 μm length and 0.1 μm thickness (*Figure 2A*).

The $\text{Na}_2\text{Ti}_3\text{O}_7$ exfoliation protocol used in this study is a modified version of previous reports for liquid exfoliation of titanates, niobates and titanoniobate nanosheets^[23] and is illustrated in *Figure 1A*. It consists of the three successive processes of swelling, exfoliation and restacking. $\text{Na}_2\text{Ti}_3\text{O}_7$ swelling was accomplished via ion-exchange steps and the effect on the interlayer spacing (d) was monitored by PXRD (*Figure 1B*), based on the position of the 001 reflection. $\text{Na}_2\text{Ti}_3\text{O}_7$ was initially ion-exchanged to its protonated $\text{H}_2\text{Ti}_3\text{O}_7$ form. Complete ion exchange was achieved, in agreement with the literature^[37],

as confirmed by ^{23}Na NMR (SI, Figure S2) and ^1H NMR (SI, Figure S3).

Although the interlayer distance (d) in the proton analogue $\text{H}_2\text{Ti}_3\text{O}_7$ ($d = 7.87$ Å) is smaller than in pristine $\text{Na}_2\text{Ti}_3\text{O}_7$ ($d = 8.46$ Å), the former is more reactive towards acid-base reactions and the layers may consequently be swollen by incorporation of protonated organic bases. This was done by ion exchange in two steps involving aqueous solutions of amines of increasing size (MA: methylamine, PA: propylamine) forming first MA- Ti_3O_7 and then PA- Ti_3O_7 . Chemical analysis (SI, Table S3, C:N ratio) confirmed that the alkyl ammonium ions were intercalated as whole ions and did not decompose under the reaction conditions. The ion exchange was complete for the first amine exchange step, while the final product after intercalation of PA ($\text{PA}_{1.7\pm 0.2}$)- Ti_3O_7 was slightly amine deficient. ^1H NMR of these materials (SI, Figure S3) confirm the presence and the stability of the alkyl ammonium ions; in the case of the PA- Ti_3O_7 , a residual amount of

protons remain in the structure bound to the Ti_3O_7 host. The yield of the exfoliation protocol strongly depends on the amount of sufficiently swollen titanate; the non-exfoliated content is removed at a later stage. The amine-driven swelling of the titanate framework results in general broadening of the reflections in the XRD patterns. The progressive shift of the 001 reflection position to lower angle indicates the increase of the interlayer spacing (d) upon intercalation of the alkyl ammonium ions ($d= 10.13 \text{ \AA}$ and 13.55 \AA for $\text{H}_2\text{Ti}_3\text{O}_7\text{-MA}$ and $\text{H}_2\text{Ti}_3\text{O}_7\text{-PA}$, respectively). Upon enlargement of the interlayer distance along the a -axis, all the (hko) reflections of $\text{Na}_2\text{Ti}_3\text{O}_7$ are expected to remain intact, with the 020 reflection at approximately 2θ (Cu K_α) = 48° being the most intense. The (001) and (020) planes of pristine $\text{Na}_2\text{Ti}_3\text{O}_7$ are displayed in *Figure 1F*.

In order to exfoliate the titanate layers/nanosheets, the amine-swollen titanate product (PA- Ti_3O_7) was dispersed in water and then sonicated. After centrifugation to remove the precipitate containing non-exfoliated material, the supernatant containing the dispersed nanosheets was

collected. The difference between the TEM of the exfoliated and the pristine material is striking. While the latter shows clearly-defined flakes and particles (SI, *Figure S4*), typical TEM images of the exfoliated (and dried) material (*Figure 1C*) are indicative of individual and multiple layers which have coalesced and collapsed as the solvent is removed, coming together in an extremely disordered arrangement with greatly reduced flake thickness. Arrays of layers can be seen in the high-contrast regions at the edges of the specimen (*Figure 1D*), but their arrangement is mostly irregular. In the regions where they form some sort of ordering, as for example at the very bottom of *Figure 1D*, no more than six layers with regular spacing are found. In these areas, the spacing between layers is in the order of $8 - 9 \text{ \AA}$, similar to the regular layer spacing observed for the pristine material, indicating the structural similarity upon removal of the solvent. The exfoliated suspension was then restacked by NaOH; a representative SEM picture is displayed in *Figure 1E* showing layers stacked in a rather disordered fashion.

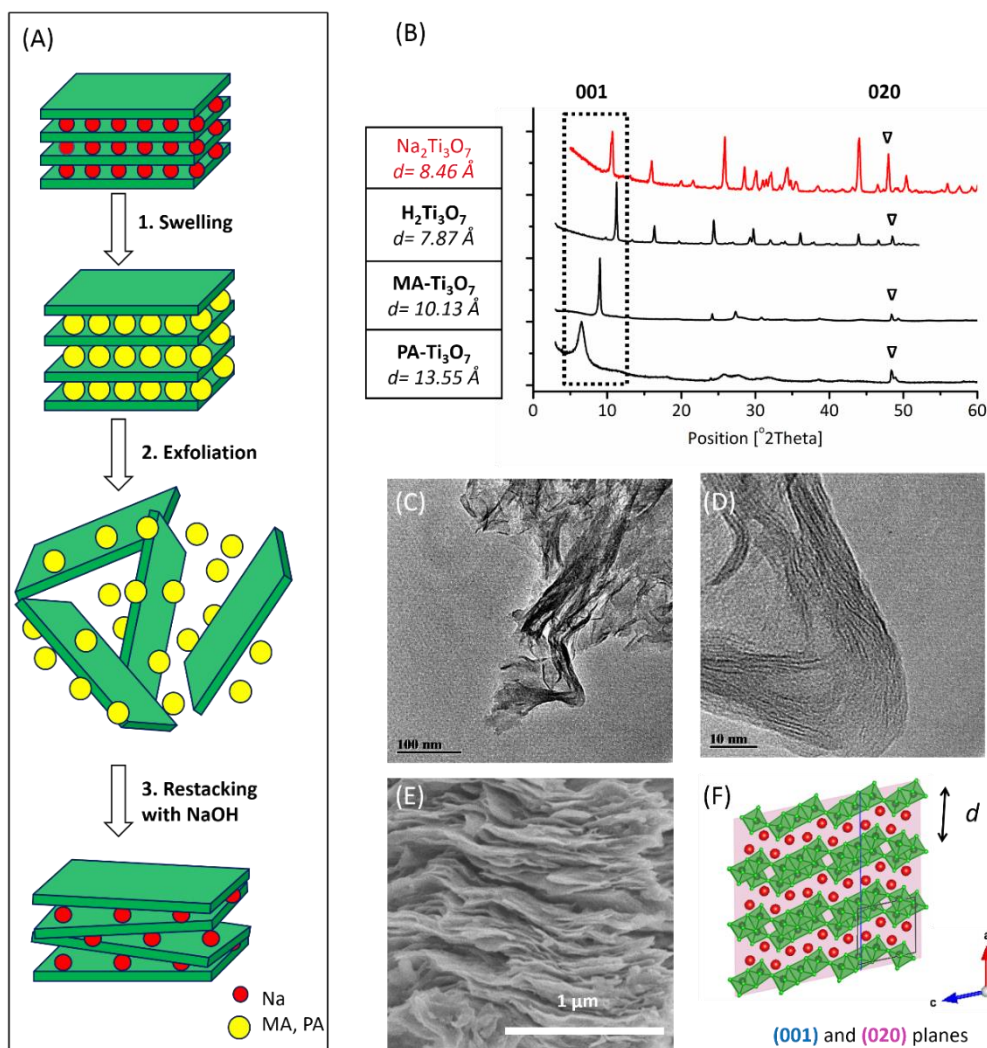


Figure 1: (A) Schematic of the exfoliation/restacking procedure, consisting of three consecutive steps: 1. swelling of pristine layered $\text{Na}_2\text{Ti}_3\text{O}_7$ by alkyl ammonium ions, by using aqueous solutions of amines of increasing size (MA: methylamine, PA: propylamine), 2. exfoliation by agitation and 3. restacking by NaOH; (B) Powder X-ray diffraction (PXRD) data monitoring the swelling, the dashed box highlighting the interlayer spacing (d), as derived from the 001 reflection. The pristine $\text{Na}_2\text{Ti}_3\text{O}_7$ was initially ion-exchanged to form the protonated $\text{H}_2\text{Ti}_3\text{O}_7$, which was then gradually swollen by ion exchange of the increasing size alkyl ammonium ions (MA, PA). The upturned triangle denotes the 020 reflection, which is retained upon swelling of the structure in the a -direction. (C, D) TEM images of exfoliated titanate nanosheet suspension, (E) representative SEM image of an exfoliated/restacked specimen, (F) Crystal structure of pristine $\text{Na}_2\text{Ti}_3\text{O}_7$, highlighting the (001) and the (020) planes, the unit cell and the interlayer distance (d). Red spheres represent Na atoms and green TiO_6 octahedra form the layered framework.

In order to control and understand the restacking process, a careful investigation of the effect of different restacking conditions was made, with two series of experiments being performed. In the first method, HNO_3 (either 1 M or 2 M) was added to the nanosheet suspension, with the obtained white precipitate separated by centrifugation. For the second method, a large excess of NaOH (aq) was added to the nanosheet solution, followed by washing under different conditions.

The morphology of the products was determined by SEM (Figure 2). The nanorods

observed for pristine ($\text{Na}_2\text{Ti}_3\text{O}_7$, Figure 2A) are still observed, but their shape is mostly irregular once the structure is swollen by the incorporation of alkyl ammonium ions ($\text{PA-Ti}_3\text{O}_7$, Figure 2B), which is the last step to exfoliation. Subsequent exfoliation and restacking changes drastically the morphology of the products, which varies according to the restacking conditions. Restacking by HNO_3 ($\text{H-Ti}_3\text{O}_7$, Figure 2C) favours the formation of aggregated nanoparticles as also evidenced by the broad PXRD patterns, with the patterns fitting quite well with those for mainly TiO_2 anatase with

some small amount of brookite (H(a)-[Ti₃O₇]) and rutile (H(r)-[Ti₃O₇]) polymorphs, for restacking by 1 M and 2 M HNO₃ respectively (SI, Figure S5). This is consistent with literature observations that different TiO₂ polymorphs can be formed hydrothermally from amorphous titania by varying the acidic conditions.^[38] The fact that TiO₂ nanoparticles are the products of the exfoliation/(nominal) restacking process by HNO₃ suggests that the drying process used

here results in structural transformation likely upon removal of structural water; this is reported to happen at temperatures above 80 °C.^[39] However, restacking by NaOH (aq) results in the formation of stacked nanosheets. The stacking order seems to be strongly dependent on the washing procedure, with reduced order observed as the samples are further washed (Figure 2D, E and F).

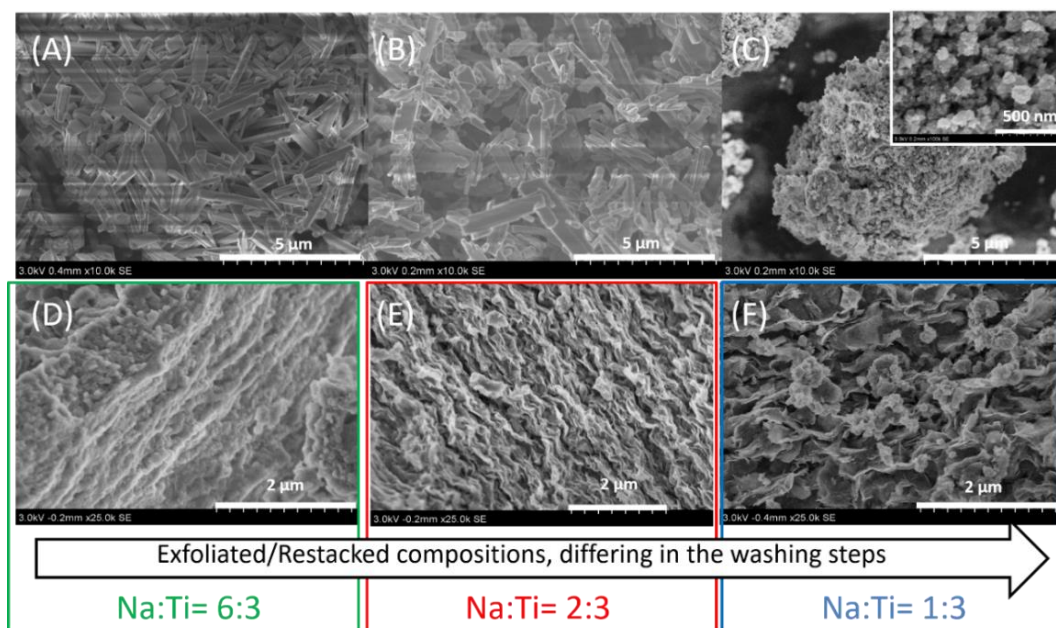


Figure 2: SEM images of (A) pristine Na₂Ti₃O₇, (B) PA-Ti₃O₇, (C) H(a)-[Ti₃O₇]; exfoliated/restacked composition by 1 M HNO₃, (D-E-F) exfoliated/ restacked compositions by NaOH, with general simplified formula Na(x)-[Ti₃O₇], showing decreased order of layers stacking with the number of washing steps. The Na:Ti ratio was measured by ICP/OES and was confirmed by converting the poorly crystalline phases to their crystalline analogues at high temperatures.

The composition of the nanosheets restacked by NaOH was first determined by ICP/OES (Table 1). The composition was also determined indirectly by converting the poorly crystalline Na(x)-[Ti₃O₇] phases at high temperatures into more well-defined crystalline phases; the Na:Ti ratio of the resulting phases as determined by PXRD (SI, Figures S6-S8) and confirmed by solid-state

NMR (SI, Figure S10) provides a second estimate of Na content (assuming all the titanate material has been converted to crystalline material). The resulting compositions were expressed via the simplified formula Na(x)-[Ti₃O₇], so as to focus only on the Na(x) content (

Table 1).

Table 1: ICP/OES results, PXRD indicating the major crystalline product identified after heating to 800 °C and composition Na(x)-[Ti₃O₇] determined from the composition of the crystalline phase.

Restacking and washing conditions	ICP (Na:Ti)	PXRD phase at 800 °C	Na(x)-[Ti ₃ O ₇]
Large excess of NaOH (aq)	1.89	Na ₂ TiO ₃	Na(6)-[Ti ₃ O ₇]
Mild washing conditions (x ₁)	0.56	Na ₂ Ti ₃ O ₇	Na(2)-[Ti ₃ O ₇]
Washed thoroughly (x ₃), pH= 7	0.29	Na ₂ Ti ₆ O ₁₃	Na(1)-[Ti ₃ O ₇]

The Na(x) content in the Na(x)-[Ti₃O₇] exfoliated/ restacked specimens was found to be approximately Na(6), Na(2) and Na(1) based on the PXRD analysis. Slightly lower Na contents were systematically determined by ICP/OES, which may be due to the techniques reported low sensitivity for Na, due to weak emission of alkali metal ions in general and interference issues for Na. ^[40] However, it may also reflect the presence of (amorphous) Na-deficient phase not seen by PXRD. The information obtained regarding

the Na(x) content of the Na(x)-[Ti₃O₇] compositions demonstrate that washing induces leaching of Na⁺ accommodated in the titanate exfoliated layers. Hence, control over washing can determine both the composition and the stacking order of the Na containing nanosheets. For easy reference, all of the exfoliated/restacked samples, and samples prepared with subsequent heat treatments and washings are listed in Table 2, along with the synthesized model compounds.

Table 2: Samples prepared in this manuscript and details of synthesis conditions

SAMPLE	COMMENT	SYNTHESIS DETAILS
Na ₂ Ti ₃ O ₇	Pristine titanate	Made by solid state synthesis at 800 °C/40 h
Formed during intermediate steps of the exfoliation protocol		
H ₂ Ti ₃ O ₇	Protonated titanate	Prepared by ion exchange of Na ₂ Ti ₃ O ₇ in HCl (aq) solution
MA- Ti ₃ O ₇	Swollen H ₂ Ti ₃ O ₇ by MA+ (MA+: CH ₃ NH ₃ ⁺)	Prepared by ion exchange of H ₂ Ti ₃ O ₇ in methylamine (MA) aqueous solution
PA- Ti ₃ O ₇	Swollen H ₂ Ti ₃ O ₇ by PA+ (PA+: CH ₃ CH ₂ CH ₂ NH ₃ ⁺)	Prepared by ion exchange of MA- Ti ₃ O ₇ by propylamine (PA) aqueous solution
As made exfoliated/restacked compositions (all dried at 100 °C in vacuum oven)		
H-[Ti ₃ O ₇]	H(a)-[Ti ₃ O ₇]: mainly anatase H(r)-[Ti ₃ O ₇]: rutile	Exfoliated and treated with HNO ₃ Drying leads to dehydration and to the formation of TiO ₂ polymorphs
Na(6)-[Ti ₃ O ₇]	Exfoliated/Restacked sample, with Na:Ti ratio=6:3	Exfoliated and restacked with large excess of NaOH (aq)
Na(2)-[Ti ₃ O ₇]	Exfoliated/Restacked sample, with Na:Ti ratio=2:3	Exfoliated and then restacked material with large excess of NaOH (aq) and washed under mild conditions
Na(1)-[Ti ₃ O ₇]	Exfoliated/Restacked sample, with Na:Ti ratio= 1:3	Exfoliated and then restacked material with large excess of NaOH (aq) and washed thoroughly
Post-treatment conditions for exfoliated/restacked compositions Na(x)-[Ti ₃ O ₇]		
Na(x)-[Ti ₃ O ₇]-400	Dried at 400 °C for 12 h and then kept in vacuum oven at 100 °C	
Na(x)-[Ti ₃ O ₇]-800	Sintered at 800 °C for 8 h and then kept in vacuum oven at 100 °C	
Model compounds made for comparison reasons		
Na ₂ Ti ₆ O ₁₃	Model compound, with Na:Ti ratio=1:3	Solid state synthesis at 800 °C/ 40 h
Na ₂ TiO ₃	Model compound, with Na:Ti ratio=6:3	Solid state synthesis at 800 °C/ 40 h

The PXRD patterns of all exfoliated/restacked $\text{Na}(x)\text{-}[\text{Ti}_3\text{O}_7]$ compositions are plotted together in Figure 3(A) and compared with those of crystalline $\text{NaOH}\cdot\text{H}_2\text{O}$ and Na_2CO_3 references, to exclude the presence of excess NaOH , as well as H_2O and CO_2 adsorption from the atmosphere. All the $\text{Na}(x)\text{-}[\text{Ti}_3\text{O}_7]$ samples display very broad reflections, demonstrating their inherent disordered nature and absence of the 001 reflection at low angles, indicating that there

is no significant ordered stacking of the layers. The PXRD pattern of the low-sodium phase $\text{Na}(1)\text{-}[\text{Ti}_3\text{O}_7]$ only displays the 020 reflection at about $48^\circ 2\theta$, which appears to be indicative of the structural coherence of the TiO_6 octahedral layered framework upon swelling (Figure 1B). This characteristic reflection is also observed in the patterns of the higher sodium containing phases $\text{Na}(2)\text{-}[\text{Ti}_3\text{O}_7]$ and $\text{Na}(6)\text{-}[\text{Ti}_3\text{O}_7]$, along with increasing amount of crystalline Na_2CO_3 .

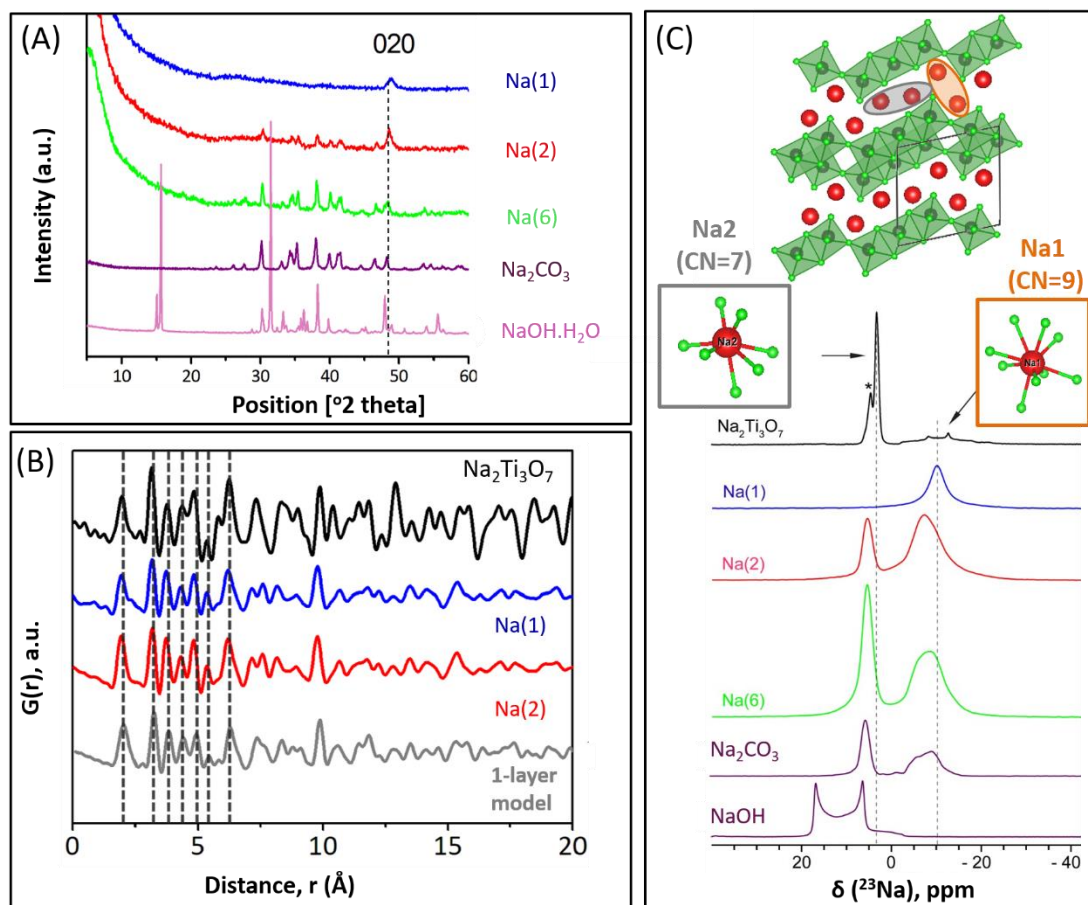


Figure 3: (A) PXRD patterns of all exfoliated/restacked $\text{Na}(x)\text{-}[\text{Ti}_3\text{O}_7]$ compositions, including $\text{NaOH}\cdot\text{H}_2\text{O}$ and Na_2CO_3 reference compounds. (B) Pair Distribution Function (PDF) analysis data for pristine $\text{Na}_2\text{Ti}_3\text{O}_7$, $\text{Na}(1)$ and $\text{Na}(2)$ compositions and comparison with the PDF pattern simulated for a single layer. Dashed lines highlight the position of low-r peaks. (C) ^{23}Na MAS NMR spectra acquired at 16.4 T for pristine $\text{Na}_2\text{Ti}_3\text{O}_7$, (highlighting the two different Na coordination environments in the structure) all exfoliated/restacked $\text{Na}(x)\text{-}[\text{Ti}_3\text{O}_7]$ compositions, NaOH and Na_2CO_3 references.

PDF analysis In order to probe the local connectivity of the exfoliated materials, pair distribution functions (PDF) were extracted from total scattering data for Na(1)-[Ti₃O₇], Na(2)-[Ti₃O₇] and the pristine Na₂Ti₃O₇. These are shown in Figure 3B. Peaks are observed in the PDF beyond 50 Å (SI, Figure S11), implying that some long-range order exists and the material is not amorphous. Peak intensity dampens more quickly with increasing distance, r , in the exfoliated material compared to the pristine material; we assign this principally to the presence of disordered interlayer correlations (i.e. between Ti₃O₇ layers) resulting in a zero contribution to the total $G(r)$. At longer interatomic distances, as the proportion of interlayer vs intralayer distances increases and, therefore, the total intensity of $G(r)$ will decrease. In addition to this, the finite size/limited coherence of the nanosheets will also contribute to the drop of intensity with increasing distance. Below 5 Å, peaks in the experimental PDF for Na(1)-[Ti₃O₇] appear at very similar distances to the pristine Na₂Ti₃O₇ material (as shown by the dashed lines in Figure 3B), indicating that the immediate connectivity of the TiO₆ framework remains the same as the parent material.

Furthermore, the peak positions in the experimental data for Na(1)-[Ti₃O₇] are a poor match to all TiO₂ polymorphs (SI, Figure S12), and the residual factors obtained from least-squares refinements of TiO₂ polymorph structures against the experimental data for Na(1)-[Ti₃O₇] are very high (SI, Table S4). This confirms that the basic exfoliation/restacking conditions have not converted the material into other TiO₂ polymorphs, as was observed in acid conditions.

To further probe the extent to which the [Ti₃O₇] layers remain intact in the exfoliated material, a model of a single [Ti₃O₇] layer, approximately 50 x 50 Å in size was constructed (SI, Figure S13(a)). Only the contributions from Ti and O are considered in the model; no Na atoms were placed in the model because the ²³Na NMR data indicate that a range of sodium environments exist (see below) and so are unlikely to contribute well-defined peaks to the PDF. Peak positions in the one-layer model show a good match to the experimental data, including the intense peak at 9.8 Å, which results from Ti-Ti interactions within the titanate layer. When this model was refined against experimental data for Na(1), a reasonable fit was obtained (SI, Figure S13 (a), $R_w = 0.39$), indicating that the structure of the exfoliated/restacked

material is similar to that of a single layer of the Na₂Ti₃O₇ parent phase.

The fit remains imperfect; peaks in the residual of the refinement ($G(r)_{\text{model}} - G(r)_{\text{experiment}}$, grey line in SI, Figure S13 (a)) remain, indicating that some aspects of the structure are not captured by the current model and, therefore, the exfoliated/restacked materials structure shows some differences to Na₂Ti₃O₇-like Ti₃O₇ layers. There are several possible sources for these differences including: (a) additional broad contributions from the disordered sodium which are not accounted for in this model; (b) the presence of some inter-layer correlations, which although likely to be disordered, may lead to some changes in intensity; (c) additional structural complexity induced by defects in the exfoliated material, and; (d) a possible range of sheet sizes and connectivities. The fit to experimental data can be slightly improved by using a fragment with smaller dimensions, where some connectivity between the corner-sharing octahedra has been broken. Of the models tried (see SI, Section S4), a fragment with extended connectivity along the b-axis, but only a single set of corner sharing octahedra shows the best fit to the data (SI, Figure S13(b), $R_w = 0.35$). This implies that some breakdown/modification of the layers may have taken place during the exfoliation/restacking, either from sheet termination, or from defective areas within sheets. However, the calculated PDF for a single unit of six edge-sharing TiO₆ octahedra, the basic building block of the Ti₃O₇ layers shows no peaks beyond approximately 10 Å (SI, Figure S13 (d)). As interatomic correlations are observed well beyond this distance in the experimental PDF, this confirms that the sheets have not been broken down into very small units of the starting material. More detailed structural characterization will be the subject of another paper.

The principal difference between the two PDFs of the two restacked compositions is the intensity of the first peak, which is likely related to the presence of a low scattering component Na₂CO₃ in Na(2)-[Ti₃O₇] (as evidenced from XRD and NMR measurements) and/or difference in the amount of oxygen vacancies present.

NMR Analysis The ²³Na NMR spectra of the three exfoliated/restacked (Na(x)-[Ti₃O₇]) compositions are shown in Figure 3C and

compared with pristine $\text{Na}_2\text{Ti}_3\text{O}_7$ and NaOH and Na_2CO_3 references. The ^{23}Na NMR spectrum of $\text{Na}_2\text{Ti}_3\text{O}_7$ consists of two signals in agreement with previously reported data^[41] and the Density Functional Theory (DFT) calculations performed in this work (SI, Figure S2). These are assigned to the two different Na coordination environments in the $\text{Na}_2\text{Ti}_3\text{O}_7$ layered structure,^[42-44] the Na_1 site at lower chemical shift (at around -10 ppm, nine-fold coordinated, coordination number (CN) = 9) with a significant second order quadrupolar broadening effect and the Na_2 site (at approximately +3.2 ppm, seven-fold coordinated, CN=7). While the spectrum of the high sodium containing $\text{Na}(6)\text{-}[\text{Ti}_3\text{O}_7]$ phase is a good match with that of the reference Na_2CO_3 spectrum, in agreement with PXRD for high carbonate content, the low sodiated $\text{Na}(1)\text{-}[\text{Ti}_3\text{O}_7]$ phase only shows a single resonance with a shift at about -10 ppm. Although not displaying the characteristic second order quadrupolar broadening, this resonance was labelled Na_1' to reflect the similarity in shift position to that of the Na_1 site (CN=9) in the pristine material. We do not necessarily assign this resonance to the same crystallographic site, but merely suggest that it has a similar CN. It is anticipated that there is some variation in the Na-O bond lengths in the disordered titanate network resulting in a distribution of slightly different chemical shifts and broader ^{23}Na NMR resonances compared to the pristine material. The intermediate sodium containing $\text{Na}(2)\text{-}[\text{Ti}_3\text{O}_7]$ phase has a spectrum that appears to correspond to a mixture of Na_2CO_3 and Na_1' , displaying the most intense shift for Na_2CO_3 at +5.5 ppm and an asymmetric resonance at lower frequency (around -9 ppm), due to the presence of overlapping carbonate and Na_1' signals.

All exfoliated/restacked compositions, display one ^1H NMR resonance with a shift at around +6 ppm (SI, Figure S14). This resonance could not be assigned to NaOH, and this signal is assigned to protons incorporated into the titanate network. $\text{H}_2\text{Ti}_3\text{O}_7$ gives rise to ^1H NMR shifts above +10 ppm (SI, Figure S3) and thus the proton signal is likely due to $\text{H}_2\text{O}/\text{H}_3\text{O}^+$ molecules/ions that are incorporated into the structure^[45] (along with residual amine groups); the slightly displaced shift of +4.8 ppm is assigned to free water molecules. Spatial constraints associated with the order of nanosheet stacking (Figure 2D-F), which is enhanced with increasing the $\text{Na}(x)$ content,

could dictate the amount of water intercalated into the titanate network.

The absence of excess NaOH in the $\text{Na}(6)\text{-}[\text{Ti}_3\text{O}_7]$ and $\text{Na}(2)\text{-}[\text{Ti}_3\text{O}_7]$ phases is explained by the observation of Na_2CO_3 , formed by reacting with H_2O and CO_2 from the atmosphere; with Na_2CO_3 presumably crystallizing on the surface upon drying. A proposed mechanism is demonstrated in SI (Figure S15), which involves the formation of a $\text{Na}_x[\text{Ti}_3\text{O}_7]^*$ metastable phase (for $x \geq 2$), which transforms to the more stable $\text{Na}(1)\text{-}[\text{Ti}_3\text{O}_7]$ phase and liberates the excess Na^+ . The excess Na_2CO_3 can cleanly be removed on washing, leaving $\text{Na}(1)\text{-}[\text{Ti}_3\text{O}_7]$ as the final stable phase. The Na atoms in $\text{Na}(1)\text{-}[\text{Ti}_3\text{O}_7]$ are accommodated in a high coordination site, additional coordination environments likely coming from bound water. (TGA and ^1H NMR indicate that this material contains approximately 2 H_2O per $[\text{Ti}_3\text{O}_7]$ unit, SI, Figure S16). The titanate framework in the as-made $\text{Na}(1)\text{-}[\text{Ti}_3\text{O}_7]$ composition is preserved as shown from the PDF analysis. In order to maintain charge neutrality in this phase, oxygen vacancies may be present or more likely, the Na ions are coordinated by both water and OH_3^+ ions, the charge compensating protons being lost as water on heating. A transition to crystalline $\text{Na}_2\text{Ti}_6\text{O}_{13}$ ($\text{Na}_1\text{Ti}_3\text{O}_{6.5}$) is expected to occur once sintered at temperatures above 600°C^[39] and is observed in this study as well when heated at 800°C (SI, Figure S8 and Figure S10 for $\text{Na}(1)\text{-}[\text{Ti}_3\text{O}_7]$) consistent to the cation ratio present in the exfoliated phase.

Electrochemistry: The exfoliated/restacked $\text{H}(x)\text{-}[\text{Ti}_3\text{O}_7]$ and $\text{Na}(x)\text{-}[\text{Ti}_3\text{O}_7]$ compositions were evaluated as anode materials for Na-ion batteries in the 0.005 -2.5 V range, at a C/20 rate (corresponding to the addition of 2 Na^+ in 20 hours). Preliminary data were also collected at C/10 and 1C for some of the compositions. The protocol initially adopted for pristine $\text{Na}_2\text{Ti}_3\text{O}_7$ with 30% carbon as a conductive additive was used for all samples to ensure consistency with the literature, and hand-grinding as opposed to mechanical milling was used to mix the reagents was used to avoid any structural rearrangement within the electrode materials.^[13] Thus, the cycling behaviour of the cell containing only carbon was also investigated for comparison. The cycling data over 20 cycles of both $\text{H}(a)$ and $\text{H}(r)\text{-}[\text{Ti}_3\text{O}_7]$ compositions are shown in Figure 4A, where closed and open symbols correspond to discharge and charge steps respectively. The first discharge capacity is notably high for both materials (≥ 1000

mAh.g⁻¹), indicating that a large amount of Na⁺ atoms are consumed irreversibly by forming the solid electrolyte interphase (SEI) layer.

Although crystallising as different TiO₂ polymorphs, both specimens demonstrate similar electrochemical performance after the initial 10 cycles, both reaching about 150 mAh.g⁻¹ after 20 cycles, at C/20 rate. During the initial 10 cycles, the capacity values diverge with slightly higher values for H(r)-[Ti₃O₇] than H(a)-[Ti₃O₇] during discharge, and converge during charge steps. The capacity values for H(r)-[Ti₃O₇], with particle size distribution between 3-10 nm (Figure 2C and SI, Figure S5), are significantly improved when compared to commercial rutile TiO₂ (Sigma Aldrich #224227, particle size < 5 μm) measured at the same conditions for this study (Figure 4B). This demonstrates

that nano-structuring TiO₂ has a significant effect on the electrochemical properties and it is the first report of nano-rutile being tested as a material for a Na-ion anode to the best of the authors' knowledge. [9, 10] Among the several TiO₂ polymorphs, the bronze-type TiO₂(B) has the most open crystal structure, followed by anatase, rutile and brookite in decreasing order, and is able to accommodate 1 Li⁺ per Ti giving a capacity of 335 mAh.g⁻¹ for Li ion batteries in both bulk and nanostructured forms^[46]; much lower capacity values are observed for sodium ion batteries due to the larger size of the Na ions.^[47] Nanosized TiO₂ typically shows poor cycling performance in Na-ion batteries; this is attributed to the formation of unstable SEI and side-reactions while cycling. [48-50]

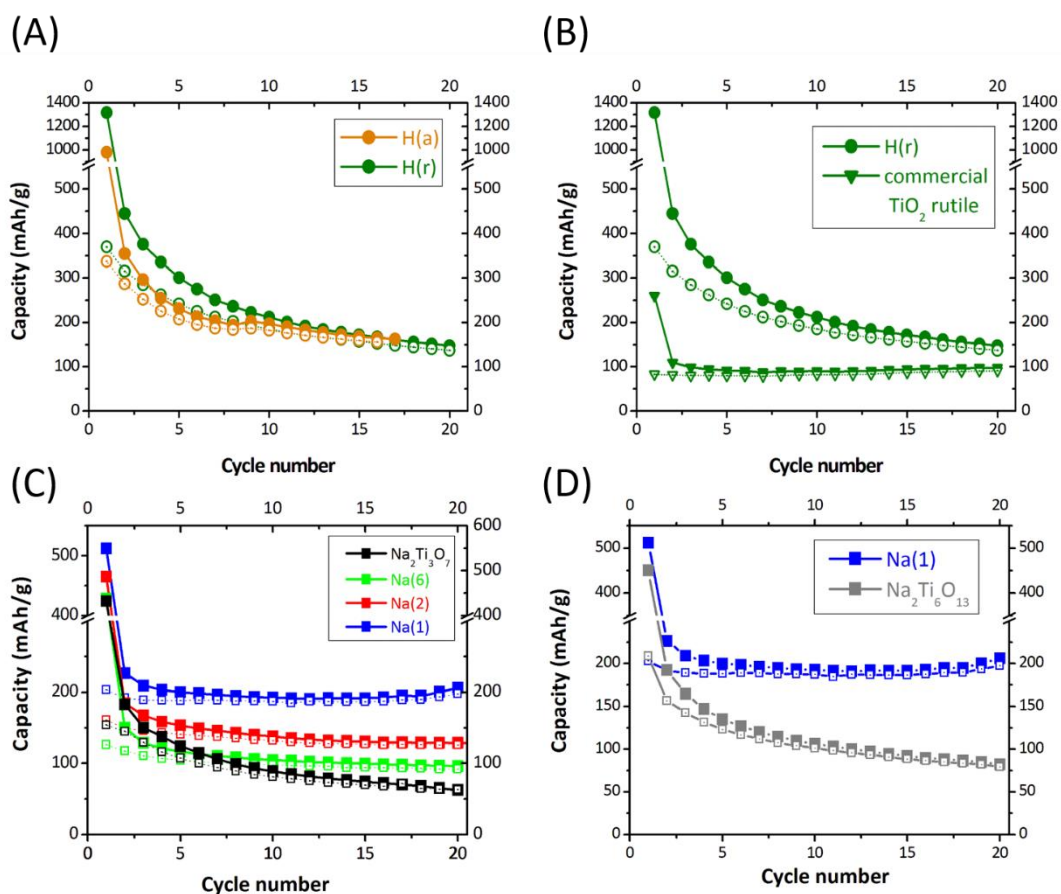


Figure 4: Cycling data over 20 cycles for (A) H(a) and H(r)-[Ti₃O₇] compositions; (B) comparison of H(r)-[Ti₃O₇] with commercial TiO₂ rutile; (C) all Na(x)-[Ti₃O₇] compositions and comparison with pristine Na₂Ti₃O₇. (D) Na(1)-[Ti₃O₇] and comparison with Na₂Ti₆O₁₃, which is the model compound with the same Na:Ti ratio. In all cases, the closed and open symbols correspond to discharge and charge steps respectively.

The cycling data over 20 cycles of Na(x)-[Ti₃O₇] compositions are shown in Figure 4C. The capacity increases with reduced Na(x) content, with Na(1)-[Ti₃O₇] displaying the best performance and attaining the highest stable capacity of about 200 mAh.g⁻¹ over 20 cycles. Despite the high first discharge irreversible capacity, similar to that obtained by other nanostructuring methods,^[17-21] all the exfoliated/restacked Na(x)-[Ti₃O₇] compositions demonstrate improved cycling performance compared to pristine Na₂Ti₃O₇, which was measured under the same conditions and suffers from poor capacity retention^[51]; this is a common problem for many potential materials used as anodes in Na-ion batteries.^[10, 52] We note however that we have not attempted to optimize the electrode formulation. Further studies would be required to understand the effect that the first cycle losses have on long-term cyclability and in full cells.

The reduced capacity values observed for the Na(2)-[Ti₃O₇] and Na(6)-[Ti₃O₇] compositions compared to Na(1)-[Ti₃O₇] are ascribed to the increasing Na₂CO₃ content. However, the presence of Na₂CO₃ in these phases is not detrimental to the properties when compared to pristine and/or the model crystalline compounds, with the same Na:Ti ratio (Figure 4D for Na(1) and SI, Figure S17(A) and S17(B) for Na(6) and Na(2) respectively). This suggests that Na₂CO₃ is inactive and the improved capacity is related to the available space for Na intercalation and the amount of the active Na(1)-[Ti₃O₇] component.

Reduction of all the Ti(IV) content would be expected to occur via the intercalation of three sodium atoms and formation of Na₅Ti₃O₇ (C_{theor}= 267 mAh.g⁻¹) during cycling. In bulk Na₂Ti₃O₇, two sodium atoms are reversibly intercalated in the structure with concomitant reduction of 2/3 of the Ti(IV) to Ti(III) in Na₄Ti₃O₇ (C_{theor}= 177 mAh.g⁻¹).^[13] The diverse values in the literature for pristine Na₂Ti₃O₇ depend largely on the formulation of the electrode, the additives and the choice of electrolyte, which has not as yet been standardized.^[52] Further optimization studies would be required to evaluate the effect of electrode formulation and processing to the capacity values measured for Na(1)-[Ti₃O₇]. At this point, it should be noted that preliminary studies on

intermediate compositions between the Na(2)-[Ti₃O₇] and Na(1)-[Ti₃O₇] end members, such as Na(ca.1.7), (SI, Figure S9 and Figure S10 for Na(ca.1.7)-[Ti₃O₇]) display higher capacities for initial cycles (e.g. about 240 mAh.g⁻¹ after 10 cycles) but these values are not stable and decrease to about 200 mAh.g⁻¹ after 20 cycles (SI, Figure S17(C)).

The galvanostatic curves of all exfoliated/ restacked Na(x)-[Ti₃O₇] compositions during the first cycle are shown in Figure 5A and compared with those of parent Na₂Ti₃O₇ and carbon cells. All the cells exhibit irreversible plateaus at about 0.6 – 1.0 V vs. Na⁺/Na and at lower voltages (0.1-0.2V) during the first discharge. These are not observed during the first charge or in subsequent cycles, demonstrated here for the second cycle (Figure 5B) and the twentieth cycle (Figure 5C). The differential dQ/dV plots are shown in SI, Figure S18. These irreversible plateaus are believed to be due to reaction of Na⁺ with the carbon additive and to the SEI formation from electrolyte decomposition.^[13, 22, 51]

It should be noted that the existence of Na₂CO₃ in the Na(2)-[Ti₃O₇] and Na(6)-[Ti₃O₇] compositions may have an additional effect on the nature of the SEI forming during operation, due to its solubility in the electrolytes commonly used for sodium-ion batteries.^[51] Moreover, the water molecules, whose existence was evidenced by ¹H NMR (SI, Figure S14), likely participate to the processes occurring at the first discharge step. These intercalated water molecules were only removed upon further drying/treatment at 400 °C (SI, Figure S16), which is likely to have an effect to the nanosheet stacking. The capacity values of Na(x)-[Ti₃O₇]-400 compositions were reduced by about 100 mAh.g⁻¹ during the first discharge step compared to as-made samples, while there was no significant difference for the subsequent cycles (SI, Figure S19). Although the incorporation of water molecules would be expected to influence the electrochemical performance while cycling by continuously reacting with the electrolyte, this was not observed for these samples under the conditions tested. It is however anticipated that the existence of intercalated water molecules might affect further high rate capability studies.

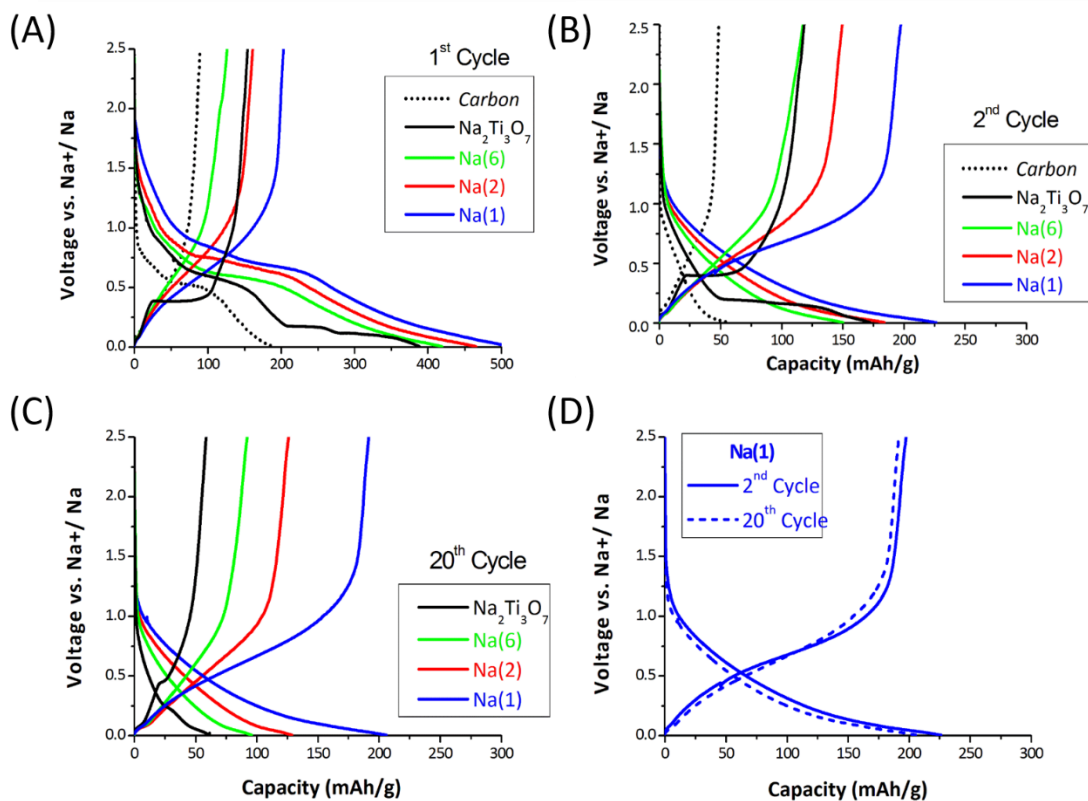


Figure 5: Galvanostatic charge/discharge curves for all exfoliated/restacked $\text{Na}(x)\text{-}[\text{Ti}_3\text{O}_7]$ compositions and comparison with pristine $\text{Na}_2\text{Ti}_3\text{O}_7$ and carbon cells, measured at the same conditions for (A) the 1st, (B) the 2nd and (C) the 20th cycles. (D) Direct comparison of the 2nd and 20th cycles for $\text{Na}(1)\text{-}[\text{Ti}_3\text{O}_7]$.

After the formation of SEI during the first discharge step, the electrochemical processes for the pristine $\text{Na}_2\text{Ti}_3\text{O}_7$ occur at distinct active sites in the bulk favoring a two-phase reaction, accompanied by flat voltage plateaus at around 0.2 and 0.4 V vs. Na^+/Na during discharge (sodiation) and charge (de-sodiation) steps, respectively^[3] (Figure 5B and Figure 5C for the 2nd and 20th cycles, respectively, dQ/dV plots in SI, Figure S18). The additional small plateau at about 0.1 V vs. Na^+/Na , observed for pristine and all exfoliated/restacked compositions, is believed to be related with the carbon additive (SI, Figure S18(D)). On the contrary, all the cells containing the exfoliated/restacked $\text{Na}(x)\text{-}[\text{Ti}_3\text{O}_7]$ compositions display sloping discharge/charge potential profiles (shown separately for $\text{Na}(1)$ in Figure 5D) compared to the pristine material, with a very broad plateau at average voltage about 0.6 V vs. Na^+/Na , most intense for $\text{Na}(1)\text{-}[\text{Ti}_3\text{O}_7]$ composition (also observed at dQ/dV plots, SI, Figure S18). This plateau is likely to be related to the existence of the Na intercalation sites (as evidenced by ²³Na

NMR, Figure 3C) and is not observed for the $\text{H-}[\text{Ti}_3\text{O}_7]$ compositions (SI, Figure S20).

In general, sloping potential profiles are indicative of single-phase behaviour, where the intercalation/deintercalation processes occur at non-equivalent sites with different energies, in part due to the disorder of these systems and the large exposed surfaces of reduced particle-size materials.^[53, 54] The overall surface area of the exfoliated/restacked materials in this study, is expected to be higher than for the pristine crystalline $\text{Na}_2\text{Ti}_3\text{O}_7$ ($\text{BET} = 1.3 \text{ m}^2 \cdot \text{g}^{-1}$); reliable BET measurements would require synthesis on a larger scale. In the general case of nano-sized materials, the intercalation/deintercalation processes are accompanied by shortened diffusion/transport distances, which is often advantageous for the overall specific capacity.^[54] For the restacked $\text{Na}(x)\text{-}[\text{Ti}_3\text{O}_7]$ nanosheets, the existence of Na intercalation sites is likely related to the observed improved capacity retention. Although higher rate data were not collected for $\text{Na}(1)\text{-}[\text{Ti}_3\text{O}_7]$, preliminary data for $\text{Na}(2)\text{-}[\text{Ti}_3\text{O}_7]$ indicate that the capacity of about $120 \text{ mAh} \cdot \text{g}^{-1}$ remains stable when cycled

at C/20 and 1C for 40 cycles (SI, Figure S20(F)). Clearly, there is further scope for optimization and high rate studies.

CONCLUSIONS

In summary, we report the exfoliation and subsequent restacking of $\text{Na}_2\text{Ti}_3\text{O}_7$ using HNO_3 and NaOH to form $\text{H}[\text{Ti}_3\text{O}_7]$ and $\text{Na}(x)[\text{Ti}_3\text{O}_7]$ compositions, respectively; these were tested as potential Na-ion anode materials. The formation of aggregated TiO_2 (rutile and anatase) nanoparticles is favoured upon drying of the $\text{H}[\text{Ti}_3\text{O}_7]$ compositions, resulting in high capacity materials, but which suffer from poor capacity retention. In the case of the $\text{Na}(x)[\text{Ti}_3\text{O}_7]$ compositions, the local connectivity of the titanate framework was retained. Control over the composition can be achieved by washing, which induces gradual Na leaching from the titanate network resulting in reduced degrees of adherence between the exfoliated layers. The final composition is $\text{Na}(1)[\text{Ti}_3\text{O}_7]$, washing removing the excess of "free/reactive" Na^+ , which otherwise forms inactive Na_2CO_3 in the insufficiently washed compositions. All the exfoliated/restacked $\text{Na}(x)[\text{Ti}_3\text{O}_7]$ compositions show significantly improved capacity retention compared to the pristine $\text{Na}_2\text{Ti}_3\text{O}_7$ and/or the crystalline compounds with the same Na:Ti ratio. This is likely related to enhanced kinetics due to nanosize effects and the formation of a more open titanate framework. The optimal electrochemical performance among the series of exfoliated/restacked $\text{Na}(x)[\text{Ti}_3\text{O}_7]$ compositions studied is demonstrated for the $\text{Na}(1)[\text{Ti}_3\text{O}_7]$ phase, where Na atoms likely occupy a range of slightly different Na intercalation sites, $\text{Na}(1)[\text{Ti}_3\text{O}_7]$ displaying a stable capacity of about 200 mAh.g^{-1} after 20 cycles at C/20 rate. In-situ and/or post-cycling studies would be required to conclude whether the intercalation of additional sodium atoms compared to pristine $\text{Na}_2\text{Ti}_3\text{O}_7$ is dominating over surface factors.

SUPPORTING INFORMATION

Further details about the characterization of materials (pristine, intermediates and products) by chemical and NMR measurements, PDF, XRD and TGA analysis, DFT calculations and TEM images, as well as supplementary electrochemical data and analysis, including Tables S1-S4 and Figures S1-S20.

NOTES

Additional data related to this publication are available at the Cambridge data repository: <https://doi.org/10.17863/CAM.18615>

ACKNOWLEDGMENTS

We thank Diamond Light Source for the provision of beam- time and access to beamline I15 (EE-14177) that contributed to the results presented here and the beamline scientists Dr. Phil Chater and Dr. Annette Kleppe. The authors thank Dr Wanjing Yu, Dr Elizabeth Castillo-Martinez and members of Cambridge Graphene Centre for useful discussions, Dr. Tao Liu for help with the SEM images and Dr. Abdul R.O. Raji for the BET measurements. M.A.T. acknowledges funding from the Engineering and Physical Sciences Research Council (EPSRC) of the United Kingdom (Grant no. EP/L019469 and EP/K01711X/1) and the EU Graphene Flagship under contract no. 604391. M.A.T, A.J.P, J.M.S and R.N.K. acknowledge funding from the United States Department of Energy (DOE, funder reference: 7057154). P.K.A. acknowledges a Junior Research Fellowship from Gonville and Caius College and an Oppenheimer Fellowship from the University of Cambridge. This project has also received funding (R.N.K) from EPSRC (Grant no. EP/K030132/1) and from the European Union's Horizon 2020 research and innovation programme under grant agreement No. 696656-GrapheneCore1 (G.K.).

REFERENCES

1. Nicolosi, V., Chhowalla, M., Kanatzidis, M. G., Strano, M. S., and Coleman, J. N., *Liquid Exfoliation of Layered Materials*. Science, 2013. **340**: p. 1226419/1-1226419/18.
2. Tan, H. T., Sun, W., Wang, L., and Yan, Q., *2D Transition Metal Oxides/Hydroxides for Energy-Storage Applications*. ChemNanoMat, 2016. **2**(7): p. 562-577.
3. Osada, M. and Sasaki, T., *Exfoliated oxide nanosheets: new solution to nanoelectronics*. J.Mater.Chem., 2009. **19**(17): p. 2503-2511.
4. Rao, C. N. R. and Nag, A., *Inorganic Analogues of Graphene*. Eur. J. Inorg. Chem., 2010. **2010**(27): p. 4244-4250.
5. Pascal, G. and Mireille, F., *Electrochemical intercalation of sodium in graphite*. Solid State Ion., 1988. **28-30**: p. 1172-1175.
6. Stevens, D. A. and Dahn, J. R., *The Mechanisms of Lithium and Sodium Insertion in Carbon Materials*. J. Electrochem Soc., 2001. **148**(8): p. A803-A811.
7. Stevens, D. A. and Dahn, J. R., *High Capacity Anode Materials for Rechargeable Sodium-Ion Batteries*. J. Electrochem Soc., 2000. **147** (4): p. 1271-1273.
8. Stevens, D. A. and Dahn, J. R., *An In Situ Small-Angle X-Ray Scattering Study of Sodium Insertion into a Nanoporous Carbon Anode Material within an Operating Electrochemical Cell*. J. Electrochem Soc., 2000. **147** (12): p. 4428-4431.
9. Kang, H., Liu, Y., Cao, K., Zhao, Y., Jiao, L., Wang, Y., and Yuan, H., *Update on anode materials for Na-ion batteries*. J. Mater. Chem. A, 2015. **3**(35): p. 17899-17913.
10. Kubota, K. and Komaba, S., *Review—Practical Issues and Future Perspective for Na-Ion Batteries*. J. Electrochem Soc., 2015. **162**(14): p. A2538-A2550.
11. Yabuuchi, N., Kubota, K., Dahbi, M., and Komaba, S., *Research Development on Sodium-Ion Batteries*. Chem. Rev., 2014. **114**(23): p. 11636-11682.
12. Wang, L. and Sasaki, T., *Titanium oxide nanosheets: graphene analogues with versatile functionalities*. Chem. Rev., 2014. **114**(19): p. 9455-9486.
13. Senguttuvan, P., Rousse, G., Seznec, V., Tarascon, J.-M., and Palacín, M. R., *Na₂Ti₃O₇: Lowest Voltage Ever Reported Oxide Insertion Electrode for Sodium Ion Batteries*. Chem. Mater. , 2011. **23**(18): p. 4109-4111.
14. Rousse, G., Arroyo-de Dompablo, M. E., Senguttuvan, P., Ponrouch, A., Tarascon, J.-M., and Palacín, M. R., *Rationalization of Intercalation Potential and Redox Mechanism for A₂Ti₃O₇ (A = Li, Na)*. Chem. Mater. , 2013. **25**(24): p. 4946-4956.
15. Li, H., Peng, L., Zhu, Y., Chen, D., Zhang, X., and Yu, G., *An advanced high-energy sodium ion full battery based on nanostructured Na₂Ti₃O₇/VOPO₄ layered materials*. Energy Environ. Sci., 2016. **9**(11): p. 3399-3405.
16. Avendano, J. M. N., *Study of Na-M-(O,F) phases: synthesis, crystal chemistry and electrochemical performance in sodium-based batteries in Chemistry Department, Faculty of Sciences 2014*, Universitat Autònoma de Barcelona
17. Ni, J., Fu, S., Wu, C., Zhao, Y., Maier, J., Yu, Y., and Li, L., *Superior sodium storage in Na₂Ti₃O₇ nanotube arrays through surface engineering*. Adv. Energy Mater., 2016. **6**(11): p. 1502568/1-1502568/8.
18. Zhang, Y., Guo, L., and Yang, S., *Three-dimensional spider-web architecture assembled from Na₂Ti₃O₇ nanotubes as a high performance anode for a sodium-ion battery*. Chem. Comm., 2014. **50**(90): p. 14029-14032.
19. Xie, F., Zhang, L., Su, D., Jaroniec, M., and Qiao, S. Z., *Na₂Ti₃O₇@N-doped carbon hollow spheres for sodium-ion batteries with excellent rate performance*. Adv. Mater., 2017. **29**(24): p. 1700989/1-1700989/6.
20. Wang, W., Yu, C., Liu, Y., Hou, J., Zhu, H., and Jiao, S., *Single crystalline Na₂Ti₃O₇ rods as an anode material for sodium-ion batteries*. RSC Adv., 2013. **3**(4): p. 1041-1044.
21. Zou, W., Li, J., Deng, Q., Xue, J., Dai, X., Zhou, A., and Li, J., *Microspherical Na₂Ti₃O₇ prepared by spray-drying method as anode material for sodium-ion battery*. Solid State Ion., 2014. **262**: p. 192-196.
22. Ko, J. S., Doan-Nguyen, V. V., Kim, H., Muller, G. A., Serino, A. C., Weiss, P. S., and Dunn, B. S., *Na₂Ti₃O₇ Nanoplatelets and Nanosheets Derived from a Modified Exfoliation Process for Use as a High Capacity Sodium-Ion Negative Electrode*. ACS Appl. Mater. Interfaces, 2017. **9** (2): p. 1416-1425.
23. Dias, A., Lima, S., Carriazo, D., Rives, V., Pillinger, M., and Valente, A., *Exfoliated titanate, niobate and titanoniobate nanosheets as solid acid catalysts for the liquid-phase dehydration of d-xylose into furfural*. J. Catal. , 2006. **244**(2): p. 230-237.
24. Filik, J., Ashton, A. W., Chang, P. C. Y., Chater, P. A., Day, S. J., Drakopoulos, M., Gerring, M. W., Hart, M. L., Magdysyuk, O. V., Michalik, S., Smith, A., Tang, C. C., Terrill, N. J., Wharmby, M. T., and Wilhelma, H., *Processing two-dimensional X-ray diffraction and small-angle scattering data in DAWN 2*. J. Appl. Crystallogr., 2017. **50**(3): p. 959-966.
25. Qiu, X., Thompson, J. W., and Billinge, S. J. L., *PDFgetX2: a GUI-driven program to obtain the pair distribution function from X-ray powder diffraction data*. J. Appl. Crystallogr. , 2004. **37**(4): p. 678-678.
26. Farrow, C. L., Juhás, P., Liu, J. W., Bryndin, D., Božin, E. S., Bloch, J., Proffen, T., and Billinge, S. J. L., *PDFfit2 and PDFgui: computer programs for studying nanostructure in crystals*. J. Phys.: Condens. Matter 2007. **19**(33): p. 33519/1-33519/7.
27. Juhás, P., Farrow, C. L., Yang, X., Knox, K. R., and Billinge, S. J. L., *Complex modeling: a strategy and software program for combining multiple information sources to solve ill posed structure and nanostructure inverse problems*. Acta Cryst. , 2015. **A 71**: p. 562-568.
28. Debye, P., *Zerstreuung von Röntgenstrahlen*. Ann. d. Physik 1915. **46**: p. 809

29. Bak, M., Rasmussen, J. T., and Nielsen, N. C., *SIMPSON: A General Simulation Program for Solid-state NMR Spectroscopy*. J. Magn. Reson., 2000. **147**: p. 296-330.
30. Pickard, C. J. and Mauri, F., *All-electron magnetic response with pseudopotentials: NMR chemical shifts*. Phys. Rev. B 2001. **63**(24): p. 245101/1-245101/13.
31. Clark, S. J., Segall, M. D., Pickard, C. J., Hasnip, P. J., Probert, M. J., Refson, K., and Payne, M. C., *First principles methods using CASTEP*. Z. Kristallogr., 2005. **220**(5-6): p. 567-570.
32. Yates, J. R., Pickard, C. J., and Mauri, F., *Calculation of NMR Chemical Shifts for extended systems using Ultrasoft Pseudopotentials*. Phys. Rev. B, 2007(76): p. 024401/1-024401/11.
33. Dirac, P. A. M., *Quantum mechanics of many-electron systems*. Proc. Royal Soc. A, 1929. **123**(792): p. 714-733.
34. Slater, J. C., *A simplification of the Hartree-Fock method*. Phys. Rev., 1951. **81**(3): p. 385-390.
35. Perdew, J. P. and Wang, Y., *Accurate and simple analytic representation of the electron-gas correlation energy*. Phys. Rev. B, 1992. **45**(23): p. 13244-13249.
36. Perdew, J. P., Burke, K., and Ernzerhof, M., *Generalized gradient approximation made simple*. Phys. Rev. Lett., 1996. **77**(18): p. 3865-3868.
37. Eguía-Barrío, A., Castillo-Martínez, E., Zarrabeitia, M., Muñoz-Márquez, M. A., Casas-Cabanas, M., and Rojo, T., *Structure of H₂Ti₃O₇ and its evolution during sodium insertion as anode for Na ion batteries*. Phys. Chem. Chem. Phys., 2015. **17**(10): p. 6988-6994.
38. Reyes-Coronado, D., Rodríguez-Gattorno, G., Espinosa-Pesqueira, M. E., Cab, R. d. C., and Oskam, G., *Phase-pure TiO₂ nanoparticles: anatase, brookite and rutile*. J. Catal., 2006. **244**: p. 230-237.
39. Bavykin, D. V. and Walsh, F. C., *Elongated Titanate Nanostructures and Their Applications*. Eur. J. Inorg. Chem., 2009. **2009**(8): p. 977-997.
40. Olesik, J. W., *Fundamental research in ICP-OES and ICPMS can result in improved performance, reliability, accuracy, and ease of use*. Anal. Chem., 1996. **68**(15): p. 469A-474A.
41. Zarrabeitia, M., Castillo-Martínez, E., López Del Amo, J. M., Eguía-Barrío, A., Muñoz-Márquez, M. Á., Rojo, T., and Casas-Cabanas, M., *Identification of the critical synthesis parameters for enhanced cycling stability of Na-ion anode material Na₂Ti₃O₇*. Acta Mater., 2016. **104**: p. 125-130.
42. Andersson, S., *The Crystal Structure of Na₂Ti₃O₇*. Acta Cryst., 1961. **14**: p. 1245-1249.
43. Yakubovich, O. V. and Kireev, V. V., *Refinement of the Crystal Structure of Na₂Ti₃O₇*. Crystal. Reports, 2003. **48**(1): p. 24-28.
44. Rudola, A., Saravanan, K., Mason, C. W., and Balaya, P., *Na₂Ti₃O₇: an intercalation based anode for sodium-ion battery applications*. J. Mater. Chem. A, 2013. **1**(7): p. 2653-2662.
45. Bavykin, D. V., Carravetta, M., Kulak, A. N., and Walsh, F. C., *Application of Magic-Angle Spinning NMR to Examine the Nature of Protons in Titanate Nanotubes*. Chem. Mater., 2010. **22**(8): p. 2458-2465.
46. Dylla, A. G., Henkelman, G., and Stevenson, K. J., *Lithium Insertion in Nanostructured TiO₂(B) Architectures*. Acc. Chem. Res., 2013. **46**(5): p. 1104-1112.
47. Huang, J. P., Yuan, D. D., Zhang, H. Z., Cao, Y. L., Li, G. R., Yang, H. X., and Gao, X. P., *Electrochemical sodium storage of TiO₂(B) nanotubes for sodium ion batteries*. RSC Adv., 2013. **3**(31): p. 12593-12597.
48. Xiong, H., Slater, M. D., Balasubramanian, M., Johnson, C. S., and Rajh, T., *Amorphous TiO₂ nanotube anode for rechargeable sodium ion batteries*. J. Phys. Chem. Lett., 2011. **2**: p. 2560-2565.
49. Wu, L., Buchholz, D., Bresser, D., Gomes Chagas, L., and Passerini, S., *Anatase TiO₂ nanoparticles for high power sodium-ion anodes*. J. Power Sources, 2014. **251**: p. 379-385.
50. Ge, Y., Jiang, H., Zhu, J., Lu, Y., Chen, C., Hu, Y., Qiu, Y., and Zhang, X., *High cyclability of carbon-coated TiO₂ nanoparticles as anode for sodium-ion batteries*. Electrochim. Acta, 2015. **157**: p. 142-148.
51. Muñoz-Márquez, M. A., Zarrabeitia, M., Castillo-Martínez, E., Eguía-Barrío, A., Rojo, T., and Casas-Cabanas, M., *Composition and Evolution of the Solid-Electrolyte Interphase in Na₂Ti₃O₇ Electrodes for Na-Ion Batteries: XPS and Auger Parameter Analysis*. ACS Appl. Mater. Interfaces, 2015. **7**(14): p. 7801-7808.
52. Ponrouch, A., Monti, D., Boschini, A., Steen, B., Johansson, P., and Palacin, M. R., *Non-aqueous electrolytes for sodium-ion batteries*. J. Mater. Chem. A, 2015. **3**(1): p. 22-42.
53. Li, D. and Zhou, H., *Two-phase transition of Li-intercalation compounds in Li-ion batteries*. Mater. Today, 2014. **17**(9): p. 451-463.
54. Liu, C., Neale, Z. G., and Cao, G., *Understanding electrochemical potentials of cathode materials in rechargeable batteries*. Mater. Today, 2016. **19**(2): p. 109-123.

TOC

